CrossMark

J. Fluid Mech. (2018), *vol.* 857, *pp.* 61–79. © Cambridge University Press 2018
doi:10.1017/jfm.2018.732

Dissolution-driven convection in a heterogeneous porous medium

Ashwanth K. R. Salibindla[1], Rabin Subedi[1], Victor C. Shen[1], Ashik U. M. Masuk[1] and Rui Ni[1,2,†]

[1]Department of Mechanical and Nuclear Engineering, Pennsylvania State University, University Park, PA 16802, USA

[2]Department of Mechanical Engineering, Johns Hopkins University, Baltimore, MD 21218, USA

(Received 29 August 2017; revised 22 August 2018; accepted 9 September 2018; first published online 15 October 2018)

Motivated by subsurface carbon sequestration, an experimental investigation of dissolution-driven Rayleigh–Darcy convection using two miscible fluids in a Hele-Shaw cell is conducted. A thin horizontal layer of circular impermeable discs is inserted to create an environment with heterogeneous and anisotropic permeability. The Sherwood number that measures the convective mass transfer rate between two fluids at the interface is linked to different parameters of the disc layer, including the disc size, spacing, layer permeability and its relative height with respect to the fluid interface. It is surprising that the convective mass transfer rate in our configuration is dominated by the disc spacing, but almost independent of either the disc size or the mean permeability of the layer. To explain this dependence, the convective mass transfer rate is decomposed into the number, velocity and density contrast of fingers travelling through the disc layer. Both the number and density contrast of fingers show dependences on the disc layer permeability, even though the product of them, the mass transfer rate, does not. In addition, the density contrast also shows a non-monotonic dependence on the disc spacing. The transition point is at a spacing that is close to the finger width. Based on this observation, a simple model based on mixing and scale competition is proposed, and it shows an excellent agreement with the experimental results.

Key words: Bénard convection, convection, convection in porous media

1. Introduction

Subsurface carbon sequestration relies on injecting CO_2 into a subsurface porous reservoir that is filled with brine, a high-salinity water. Buoyant CO_2 will rise in heavier brine and eventually return to the atmosphere, unless this motion is hindered by a caprock – a layer of rock with low permeability that CO_2 cannot penetrate through. Below the caprock, CO_2 can only spread horizontally, resulting in a two-layer system with CO_2 above brine. At the interface, CO_2 slowly dissolves into brine and the density of the mixture is higher than that of each individual fluid alone, thereby leading to an unstable configuration with a heavier fluid on top of a lighter one and triggering the convection process (Huppert & Neufeld 2014).

† Email address for correspondence: rui.ni@jhu.edu

https://doi.org/10.1017/jfm.2018.732 Published online by Cambridge University Press

Convection in a porous medium is also known as Horton–Rogers (Horton & Rogers 1945), Lapwood (Lapwood 1948), Darcy–Bénard (Rees & Bassom 2000) or Rayleigh–Darcy (Nield 1983) convection, and many of these problems were discussed primarily in the context of thermal convection, in which the density gradient is driven by the temperature difference. Similar to thermal convection, dissolution of CO_2 into brine leads to a growing diffusive boundary layer that is similar to the thickening thermal boundary layers (Foster 1965). When this diffusive layer becomes thick enough, any small perturbation will trigger the convection process. Two key dimensionless parameters to describe convection are the Rayleigh number (Ra) and the Sherwood number (Sh). The Rayleigh number is a measure of the strength of convection (Nield & Bejan 2006), and the Sherwood number is used to quantify the dissolution mass transfer rate. Typically, Sh is larger than one, which represents the enhancement of dissolution due to convection compared with the diffusive process alone (for details, see § 2).

Rayleigh number determines the flow regime. Below a critical Rayleigh number Ra_c, no instability is sustainable. This Ra_c is roughly from 31.5 (Slim 2014) to 32.5 (Slim & Ramakrishnan 2010) based on analytic approximation and linear stability analysis. For Ra much larger than 32.5 but smaller than $O(10^3)$, numerical studies show that the process is transient, developing from diffusive, early convective and eventually to late convective mixing periods (Meybodi & Hassanzadeh 2013). For a large $Ra > O(10^3)$, the flow switches to the 'high-Ra' regime (Otero *et al.* 2004; Backhaus, Turitsyn & Ecke 2011; Hewitt, Neufeld & Lister 2012). In this regime, after the onset of the instability and before the saturation of dissolved CO_2 in brine, the mass flux appears to be constant over a period of time and Sh exhibits a power-law relationship with Ra: $Sh = \alpha\, Ra^n + \beta$ (Hassanzadeh, Pooladi-Darvish & Keith 2007; Hidalgo & Carrera 2009; Pau *et al.* 2010). This has stimulated interest and debate around this problem as to whether the Sh–Ra relationship is linear ($n = 1$) (Pau *et al.* 2010; Elenius & Johannsen 2012; Slim 2014) or sub-linear ($n \approx 0.8$) (Neufeld *et al.* 2010; Backhaus *et al.* 2011; Farajzadeh *et al.* 2013). As an attempt to address this issue, Hidalgo *et al.* (2012) utilized theoretical analyses and simulations to attribute the observed difference to the nonlinear density–concentration dependence of the mixture. For a canonical Rayleigh–Darcy convection with a linear density–concentration dependence, the Sh–Ra dependence is suggested to be linear ($n = 1$). However, most laboratory experiments typically use analogous fluids such as water–methanol ethylene glycol (MEG) (Neufeld *et al.* 2010) and water–propylene glycol (PPG) (Backhaus *et al.* 2011; Agartan *et al.* 2015) mixtures. In these systems, mixture density exhibits a non-monotonic dependence on the concentration, and this is believed to be a possible reason for the sub-linear Sh–Ra dependence observed in many experiments.

These past works on the Sh–Ra relationship provide baseline measurements of the convective mass transfer in a homogeneous porous medium with a uniform permeability and porosity. These results cannot, however, be used directly to model subsurface carbon sequestration in a geological environment that exhibits a wide distribution of permeability and porosity across many different length scales. This motivates several studies to focus on the effects of heterogeneity and anisotropy of the permeability distribution on the critical Rayleigh number and onset of convection (McKibbin & O'Sullivan 1980; Ennis-King, Preston & Paterson 2005; Xu, Chen & Zhang 2006; Rapaka *et al.* 2009; Cheng, Bestehorn & Firoozabadi 2012). By using the linear and global stability analyses, it was shown that both the critical Rayleigh number and onset time increase as the anisotropy ratio decreases, indicating that the gravitational instability tends to be stabilized by the additional anisotropy of the permeability distribution (Ennis-King *et al.* 2005).

https://doi.org/10.1017/jfm.2018.732 Published online by Cambridge University Press

For Ra larger than the critical value, the convection pattern and mass (heat) transfer rate have been linked to three distinct types of heterogeneity and anisotropy, including (i) one or multiple low-permeability layer(s) sandwiched in an otherwise homogeneous environment (McKibbin & O'Sullivan 1981; Rees & Riley 1990; Rees & Genç 2011; Agartan *et al.* 2015), (ii) many small thin barriers following certain statistics (Farajzadeh *et al.* 2011; Green & Ennis-King 2014), or (iii) a distribution of permeability assigned to each grid of the volume (Green & Ennis-King 2014). All three types of configurations are motivated by certain features of geological environments. For instance, the layered structure is the most common large-scale heterogeneity in sedimentary formations, and the world's first CO_2 storage facility located in Sleipner offshore of Norway has several layers of low-permeability rocks in the entire reservoir (Cavanagh & Haszeldine 2014). In these configurations, different flow patterns appear in different layers (McKibbin & O'Sullivan 1981; Agartan *et al.* 2015), and the overall dissolution rate depends on the permeability ratio between two layers (Hewitt, Neufeld & Lister 2014). For the other two types of methods, the focus is more on the local permeability variations. The Dykstra–Parsons coefficient was utilized to quantify the permeability distribution (Farajzadeh *et al.* 2011). Depending on the range of this coefficient and the correlation length of the spatial distribution of permeability, it was shown that the dynamics of convection at $Ra = 5000$ can be separated into three regimes: gravity fingering, channelling and dispersive regimes.

When both the large-scale layered structure and small-scale permeability variation are present in a porous medium, the question arises as to what the best way is to quantify the effect of different types of heterogeneity and how to connect that to the convective mass transfer rate. In this paper, we designed a simple experiment by inserting a layer of impermeable discs into an otherwise homogeneous medium. This design imposes two different types of heterogeneity: (i) the entire layer has a lower mean permeability than the remaining medium (large scale), and (ii) within this layer, there are alternate low and high permeabilities (small scale). The simple geometry can also serve as a building block towards a more sophisticated permeability distribution, and it will help us to gain more insights into the problem of convection in a porous medium with heterogeneous permeability across different scales.

In § 2, we will introduce the fluid properties, Hele-Shaw cell, impermeable discs and definitions of the various dimensionless numbers. In § 3, we provide details of the experimental procedure, from setting up the experiments to data acquisition and analysis. In § 4, the discussions are divided into several subsections to study convective mass transfer and its relationship with different parameters and length scales introduced by the disc layer. In addition, a model is proposed to explain some surprising results. All the experimental results, possible future research directions, and implications from our research are summarized in § 5.

2. Experimental set-up and parameters

Conducting a laboratory experiment of supercritical CO_2 and brine at an elevated pressure (100 bar) will help to preserve the physicochemical properties of these two fluids, but this type of high-pressure experiment is inherently challenging. This motivates us to use an analogous fluid system, which maintains the key physics of the dissolution convection but allows for simpler experimental protocols. In this study, water and PPG are adopted to replace CO_2 and brine (Backhaus *et al.* 2011). This combination is similar to the CO_2–brine system, in which the density of the mixture can be greater than the density of either fluid alone. As shown in figure 1,

https://doi.org/10.1017/jfm.2018.732 Published online by Cambridge University Press

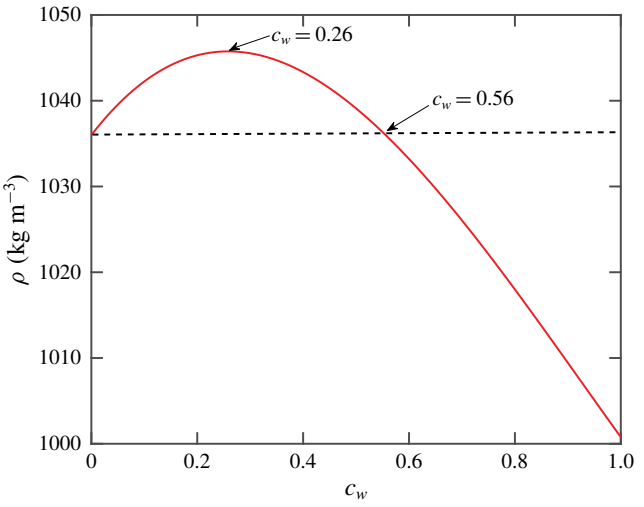


FIGURE 1. (Colour online) Density of water–PPG mixture as a function of the volume fraction of water (c_w).

the mixture density is related to the water concentration c_w via an empirical equation (Hewitt 2014):

$$\rho_i = 64.232c_w^3 - 179.228c_w^2 + 79.772c_w + 1036.0 \text{ kg m}^{-3}. \tag{2.1}$$

The dashed line in figure 1 indicates the density of pure PPG, and it is clear that the mixture density with volume fraction of water in the range of $0 < c_w < 50\,\%$ is indeed larger than that of pure PPG. The density–concentration curve appears to be nonlinear and might lead to a sub-linear *Sh–Ra* relation (Szulczewski, Hesse & Juanes 2013; Emami-Meybodi *et al.* 2015). But its effect on our study should be secondary, as our study intends to keep a constant Rayleigh number in order to isolate the effect of permeability distribution.

As shown in figure 2, a vertically oriented Hele-Shaw cell made of two pieces of borosilicate glass is used to make sure that the flow in this system obeys Darcy's law. A U-shaped metal frame with a uniform thickness b and an inner dimension of 76 mm $\times$ 76 mm was placed between two pieces of glass to set the gap width and the boundaries for the fluids within. Two frames with $b = 0.254$ or 0.508 mm were used to vary the permeability, $k = b^2/12$. This type of set-up with a uniform permeability is henceforth referred to as the *homogeneous* configuration. A thin metal shim is used to separate water and PPG when filling the Hele-Shaw cell, and it also sets the water–PPG interface location and the height of the PPG layer H. Two different heights, $H =$ 20 and 50 mm, were used. When the system is ready, the metal shim will be slowly pulled away to allow the two fluids to come into contact with each other and trigger the convection process (Backhaus *et al.* 2011).

To introduce the heterogeneous permeability across multiple length scales, circular latex discs with identical sizes were cut by a laser cutter and inserted into the Hele-Shaw cell. Discs were aligned in a horizontal layer. In this study, we used three different disc sizes, $D = 2.5$, 3.5 and 4.5 mm. The thickness of the discs matches the gap of the Hele-Shaw cell, thereby completely blocking flows and creating a region with zero permeability. This arrangement introduces three new length scales: disc

https://doi.org/10.1017/jfm.2018.732 Published online by Cambridge University Press

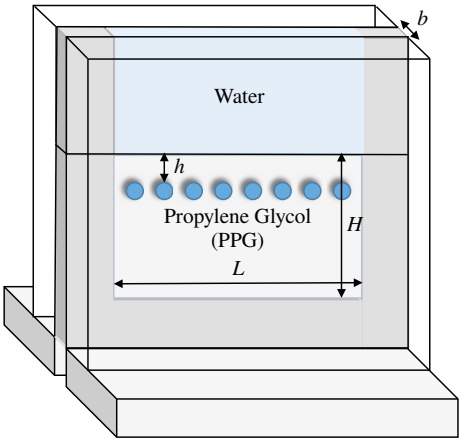


FIGURE 2. (Colour online) Schematic illustration of the vertical Hele-Shaw cell with a layer of discs inserted to create an environment with a heterogeneous and anisotropic permeability distribution.

size (D), disc spacing (l) and disc–interface distance (h). It also features two different types of heterogeneity: a horizontal layer with low mean permeability extended to the whole cell width L, and local permeability variations from zero (discs) to the background permeability k (between discs) at a length scale D. The dependence of the dissolution rate on D and l will be introduced in § 4.2.2 and its dependence on h will be discussed in § 4.2.3.

Similar to previous work (Backhaus *et al.* 2011), at the interface, c_w is assumed to be a constant at 0.15, with the density of the mixture $\rho_i = 1.044$ g cm^{-3} based on (2.1). This density is larger than that of the underlying PPG, and the density difference is $\Delta\rho = \rho_i - \rho_{PPG} = 0.009$ g cm^{-3}. Driven by gravity, a heavy mixture finger will descend into the PPG layer with a terminal velocity $v_c = \Delta\rho g k/\rho_i \nu$. As the entire process is dominated by convection, v_c is also referred to as the convective velocity. With such velocity, it takes convection approximately a time $t_c = H/v_c$ to travel the entire PPG layer with height H. On the other hand, if the mass is transported solely by diffusion, it would take the mixture approximately $t_d = H^2/D_m$ to pass a distance of H at a diffusive velocity $v_d = D_m/H$, in which $D_m = 10^{-6}$ cm^2 s^{-1} is the mass diffusivity (Hubel, Bidault & Hammer 2002). The Rayleigh number can be calculated using the ratio between these two velocities:

$$Ra = v_c/v_d = \Delta\rho g H k/\rho_i \nu D_m, \tag{2.2}$$

with $\nu = 0.1$ cm^2 s^{-1} (Rahbari-Sisakht, Taghizadeh & Eliassi 2003) being the viscosity of the mixture. Both D_m and ν are assumed to be constants in this study.

The dimensionless mass transfer rate is defined as the Sherwood number, $Sh = \dot{m}/\rho(D_m/H)bL$, the ratio between the total mass flux $\dot{m}$ and the diffusive mass flux. It is challenging to directly measure the value of mass flux, $\dot{m}$, from experiments, so it is indirectly estimated from the interfacial velocity, $v^* = \mathrm{d}H^*/\mathrm{d}t^*$. Here H^* is the dimensionless height of the PPG layer at each time instant. Then Sh is formulated as the product of Ra and the interfacial velocity:

$$Sh = (\mathrm{d}H^*/\mathrm{d}t^*)Ra, \tag{2.3}$$

with a dimensionless time scale $t^* = t/t_c$.

https://doi.org/10.1017/jfm.2018.732 Published online by Cambridge University Press

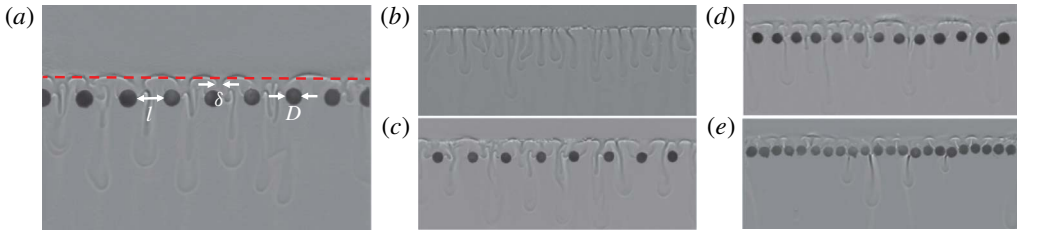


FIGURE 3. (Colour online) Shadowgraph images of dissolution-driven convection in a vertical Hele-Shaw cell with (*a*) $D = 5.63$ mm and $l = 1.64$ mm, (*b*) no discs, and (*c–e*) $D = 2.5$ mm and $l = 4.8$, 2.2 and 0.47 mm, respectively. The interface location in (*a*) is marked with a dashed red line that is extracted using the method introduced in § 3.

3. Experimental procedure

Before each experiment, all the components of the Hele-Shaw cell were cleaned and dried using compressed air to prevent contaminated surfaces from trapping small bubbles. The U-shaped metal frame was placed on the surface of one piece of glass. A layer of discs was then positioned at the designated location. After that, the other piece of glass was clamped on, and the edge of the frame was sealed with vacuum grease to complete the set-up. The entire cell was then oriented vertically so that it could be filled with fluids. PPG was injected slowly into the cell until it reached the level of a metal shim; the shim was used to separate the two fluids and any excess PPG above the shim was removed using a dry tissue. Finally water was injected following the same procedure, and the set-up was ready. The camera began to record when the shim was slowly pulled away to start an experiment.

Light is generated from a fibre optic light source and condensed through a Fresnel lens. The shadow of the flow structures was projected onto a Mylar sheet and recorded by a camera at two frames per minute over seven hours. Raw images were processed to remove background. The results are shown in figure 3(*a–e*), and interface and fingers are clearly visible. The interface appears to be a straight line extended horizontally with a strong contrast for all disc configurations, from no discs (*b*) to discs with tight spacing (*e*). The vertical intensity profiles for one configuration (figure 3(*a*)) at different times are shown in figure 4(*a*). This profile is acquired directly from the shadowgraph image by averaging vertical lines of pixels in the entire image along the horizontal direction. The interface location can be determined from the peak of the intensity profile. To validate this method, the interface position from this method is shown in figure 3(*a*) as a dashed red line, which clearly overlaps with the interface. The interface moves as a function of time, and their relationship appears to be linear for a long time, as shown in figure 4(*b*). The blue solid line in figure 4(*b*) indicates a linear fit, which collapses perfectly with the data points. This linear relationship implies that a constant-flux regime exists even for a heterogeneous porous medium. The slope of this linear curve was used to calculate the mass transfer rate ($\mathrm{d}H^*/\mathrm{d}t^*$) and the Sherwood number, $Sh = (\mathrm{d}H^*/\mathrm{d}t^*)Ra$.

4. Experimental results

4.1. *A homogeneous medium*

The baseline experiments to validate our experimental procedure are to measure the *Sh–Ra* relationship in a homogeneous medium with no discs. The *Ra* value is chosen to be around 10^4 (Neufeld *et al.* 2010). Two different heights, $H = 20$ and

https://doi.org/10.1017/jfm.2018.732 Published online by Cambridge University Press

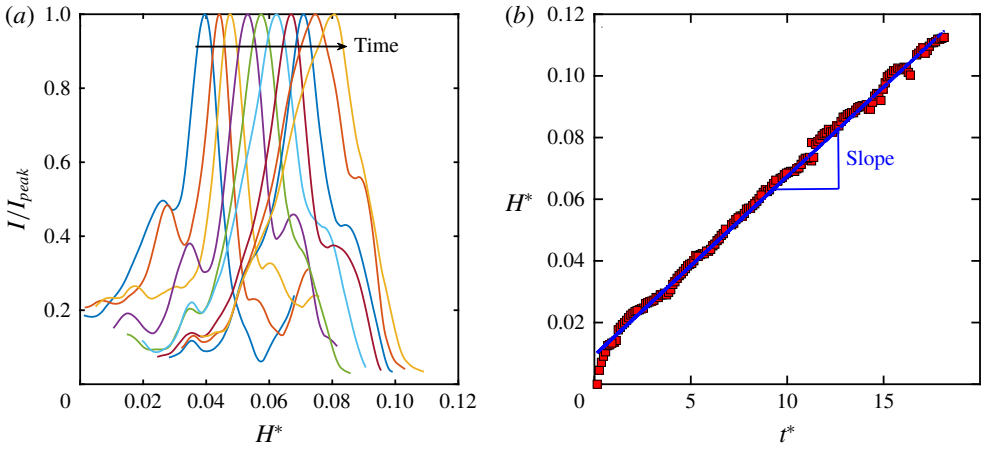


FIGURE 4. (Colour online) (*a*) Normalized intensity profile across the interface at different time steps extracted from shadowgraph images (figure 3*a*). (*b*) Extracted peak positions from (*a*) versus the normalized time $t^* = t/t_c$. The solid blue line shows a linear fit to the symbols.

50 mm, and two different gap widths, $b = 0.254$ and 0.508 mm, were used to cover a range of $Ra = 10^4$–10^5. The *Sh*–*Ra* relationships obtained from our experiments were compared with several previous datasets as shown in figure 5. Both the degree of data scatter and the scaling exponent of *Sh*–*Ra* in our experiments are very close to those of a previous experiment in a similar configuration (Backhaus *et al.* 2011), but *Sh* from our experiments are systematically higher. To rule out the possibility of contaminated fluid or batch difference, propylene glycol purchased from different vendors (Essential Depot, Dow Chemicals) and different types of water, including tap water and distilled water, were used. It turns out that using tap water will lead to approximately 11 % overestimation of the mass dissolution rate. But as long as distilled water is used, the reproducibility of our experiment remains in the 6.5 % range, including two different types of PPG that we used. In sum, this uncertainty due to fluid contamination or batch difference cannot explain the systematic shift between our dataset and the previous work (Backhaus *et al.* 2011). Although our *Sh* are larger, they are still within the range bounded by two different experiments by Neufeld *et al.* (2010) and Backhaus *et al.* (2011), and our results appear to be closer to simulation results from Otero *et al.* (2004). Although the focus of this study is not on the Rayleigh-number dependence, these measurements mark the baseline of dissolution-driven convective mass transfer in a homogeneous medium.

4.2. *A heterogeneous medium*

4.2.1. *The Sherwood number*

Adding a layer of impermeable discs will reduce the permeability. The disc layer permeability k_l is quantified using simulations (for details, see Appendix), and it is found that $k_l/k \approx l/(l + D)$, where k represents the permeability of the rest of the cell with no discs. Since the disc layer represents only a small portion of the PPG layer, the addition of such a layer affects the mean bulk permeability by less than 10 %. This will translate to ∼10 % change of the Rayleigh number, which is small enough that it does not affect the *Sh* significantly. In a previous work

https://doi.org/10.1017/jfm.2018.732 Published online by Cambridge University Press

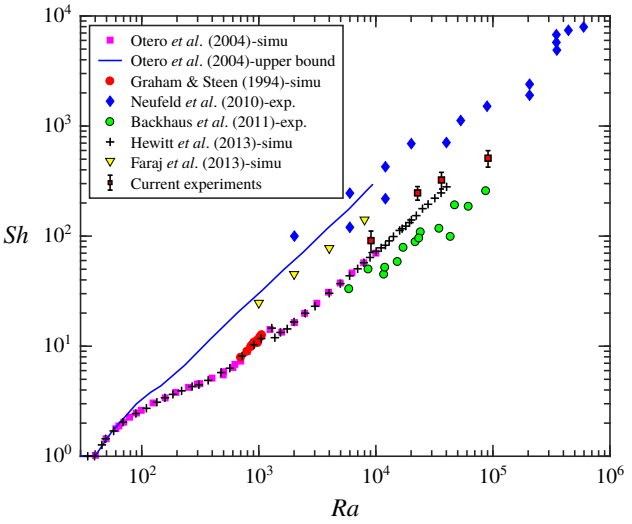


FIGURE 5. (Colour online) Compilation of *Sh–Ra* in a homogeneous porous medium from previous simulations and experiments, together with a few data points from the current work.

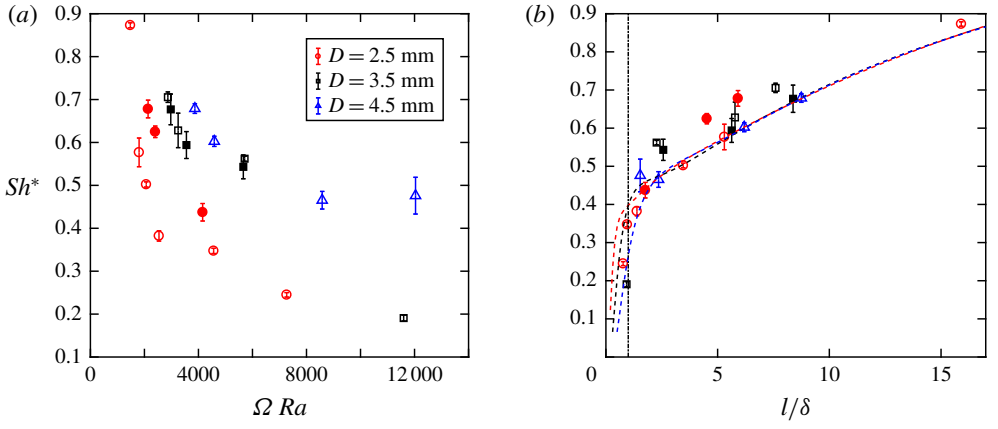


FIGURE 6. (Colour online) (*a*) Normalized Sherwood number Sh^* as a function of $\Omega\, Ra$ for various disc sizes at $Ra = 9.87 \times 10^3$ (solid markers) and 2.27×10^4 (open markers). (*b*) Plot of Sh^* versus normalized disc spacing l/δ. The vertical dash-dotted line marks $l/\delta = 1$. The dashed lines show our model predictions (for details, see § 4.2.2).

(Hewitt *et al.* 2014), the dimensionless impedance, $\Omega = (D/H)/(k_l/k)$, was defined to quantify the addition of a low-permeability layer. The same method is adopted here to test if the mean permeability of the disc layer is the controlling parameter.

To help with the discussion, the Sherwood number from a heterogeneous medium, Sh_{het}, was normalized by its homogeneous counterpart, Sh_{hom}, i.e. $Sh^* = Sh_{het}/Sh_{hom}$, which ranges from zero to one. Two different heights H of the PPG layer allow us to have two different Rayleigh numbers, $Ra = 9.87 \times 10^3$ and $Ra = 2.27 \times 10^4$. Figure 6(*a*) shows Sh^* as a function of $\Omega\, Ra$. In addition to Ω, Ra is added

https://doi.org/10.1017/jfm.2018.732 Published online by Cambridge University Press

to compensate for the systematic shift of datasets from two different Rayleigh numbers (open and closed symbols). Although Ω helps to collapse all datasets in a simulation (Hewitt *et al.* 2014), it does not work for our experiments with different disc configurations, as shown in figure 6(*a*). Note that there are two features of our experimental configuration that differ from the numerical set-up: (*a*) the simulation is on two-sided thermal convection, whereas our experiment focuses on one-sided dissolution-driven convection; and (*b*) the permeability within the inserted layer in the numerical configuration is uniform, whereas our low-permeability layer consists of alternating low- and high-permeability zones.

The dimensionless impedance Ω is a function of two new length scales, D and l. Since Ω does not work, we decided to take a step back and study the dependence of Sh on either D or l alone. Figure 6(*b*) shows Sh as a function of l. In figure 6(*b*), l is normalized by a constant δ, which represents the width of mixture fingers developed from the interface; δ is measured directly from the shadowgraph images by extracting the width of a finger at around 0.6–0.7 mm away from the interface. Even though the finger width will continue to grow as fingers descend, we chose to quantify the finger width at this fixed location because it is where the fingers have the best contrast and the smallest width. The same measurements of δ were repeated in all disc configurations, and δ is found to be a constant at 0.63 mm in all disc configurations. In figure 6(*b*), a collapse of all data points suggests that l/δ might be a better parameter to characterize the heterogeneity for our configuration. These data points share one trend: Sh^* decreases with decreasing l, and it drops sharply at $l/\delta \approx 1$. This is because l/δ characterizes two different flow regimes: convective fingers freely pass through the gap for $l/\delta > 1$, and no finger directly passes through the gap for $l/\delta < 1$. The surprising part is that the results show weak dependence, if at all, on D, at least in the range of D that we used. Note that D represents the distance between two high-permeability channels as well as the thickness of the disc layer. This finding may have important implications to subsurface carbon sequestration. For example, if the geological formation has some low-permeability layers filled with fractures (high-permeability gaps), it is possible that the fracture width is the dominant factor that controls the convective flow, and fracture–fracture distance and layer thickness are secondary.

4.2.2. *Model*

Convective mass transfer is primarily conducted by descending mixture fingers. Based on this argument, the convective mass transfer rate $\dot{m}$ can be expressed as a function of the number n_f, width δ, thickness b, velocity u_f and density ρ of these fingers, $\dot{m} = \rho b c_w u_f n_f \delta$. Combined with the definitions of Sh and Ra, it is found that $Sh = c_w n_f (\delta/L)(u_f/u_c) Ra$, which depends primarily on the volume fraction of fingers in the PPG layer, $n_f \delta/L$, and the dimensionless finger velocity, u_f/u_c (Backhaus *et al.* 2011).

In $n_f \delta/L$, n_f represents the number of fingers that pass through the disc layer. Since δ/L is a constant, the entire term is controlled by n_f. This number can be directly extracted from shadowgraph images by counting the number of fingers right below the disc layer. From these images shown in figure 3(*b–e*), it is obvious that n_f increases as l becomes larger, consistent with what one would expect. Figure 7(*a*) shows n_f as a function of l/δ for different disc sizes, and the error bar indicates the variation of n_f for each configuration. To our surprise, l/δ does not work to collapse all datasets for n_f, even though l/δ was proven to be the parameter to quantify the heterogeneity effect for Sh.

https://doi.org/10.1017/jfm.2018.732 Published online by Cambridge University Press

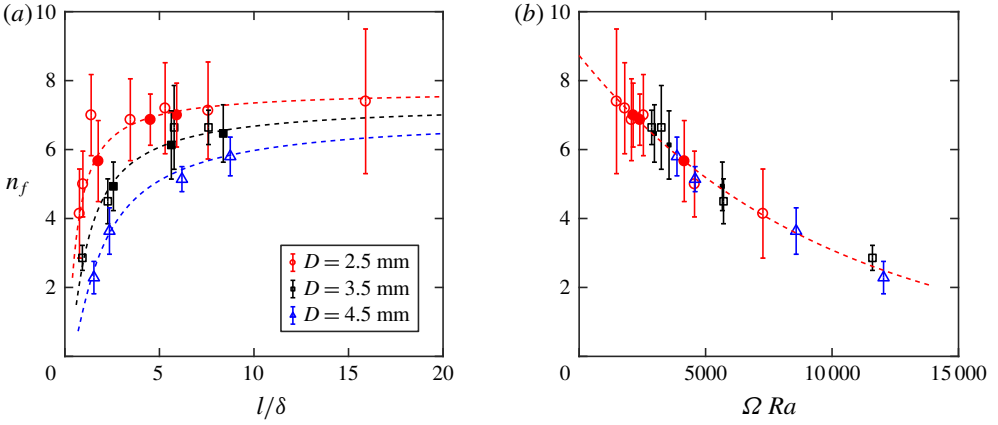


FIGURE 7. (Colour online) (*a*) Number of fingers (n_f) versus normalized disc spacing l/δ at $Ra = 9.87 \times 10^3$ (solid markers) and 2.27×10^4 (open markers). The three dashed lines correspond to the single dashed line in (*b*). (*b*) Plot of n_f versus $\Omega\, Ra$ for the same datasets. The dashed line represents an exponential fit over all data points.

More surprisingly, the impedance $\Omega\, Ra$, which failed for Sh, perfectly explains the dependence of n_f, as shown in figure 7(*b*). The dashed line in figure 7(*b*) shows an exponential fit of all data points: $n_f = a\exp(-b\Omega\, Ra)$, in which $a = 8.73$ and $b = 1.04 \times 10^{-5}$. This function bridges two known limits at $\Omega = 0$ (no discs with zero gaps) and $\Omega = \infty$ (touching discs with zero gaps). At $\Omega = 0$, n_f is equal to 8.73, a number that is consistent with the one obtained in a homogeneous medium (Backhaus *et al.* 2011). When Ω approaches infinity, the layer is completely closed, and no fingers can pass, i.e. $n_f = 0$. This nice collapse of all data points onto one curve implies that n_f is controlled primarily by the permeability (or impedance), rather than by the disc spacing l.

Convective mass transfer is also affected by the finger velocity u_f. Fingers moving downwards at a speed of u_f will drive pure PPG between fingers to move upwards at a speed of u_b. The values of u_f and u_b are related to the number of fingers $u_f\delta = (L/n_f - \delta)u_b$, where L/n_f represents the average finger spacing. They are also related to the convective velocity u_c through a path integration of Darcy's law through a finger and a back-flow: $u_c = u_f + (\nu_{PPG}/\nu_w)u_b$. This will eventually lead to a new equation, $u_f/u_c = 1/[1 + (\nu_{PPG}/\nu_w)(n_f\delta/L)/(1 - (n_f\delta/L))]$, directly linking u_f/u_c to n_f (Backhaus *et al.* 2011). As shown in figure 8(*a*), the calculated u_f/u_c shows a weak dependence on l/δ. To confirm the result, an independent method from image analysis can be used to directly extract the velocity of fingers u_f (Ecke & Backhaus 2016). The vertical finger velocity is determined from a sequence of images, as shown in the inset of figure 8(*b*). The results of measured u_f normalized by u_c, assuming a constant density contrast, are shown in figure 8(*b*). Similar to a previous work (Ecke & Backhaus 2016), the variations of finger velocity, indicated by the error bars, are large, and it is difficult to draw a conclusion about the dependence of u_f on l/δ or $\Omega\, Ra$ with these uncertainties. If there is any trend at all, both methods confirm that the normalized finger velocity u_f/u_c does not change much over different disc configurations.

The analyses so far raise an important issue: if $Sh = c_w n_f(\delta/L)(u_f/u_c)Ra$ holds, n_f is a function of Ω, and c_w, u_f/u_c and Ra are all (close to) constants, then Sh should also depend on Ω, which is inconsistent with our findings that Sh depends on l/δ rather than on Ω. This suggests that one parameter that was assumed to be constant

https://doi.org/10.1017/jfm.2018.732 Published online by Cambridge University Press

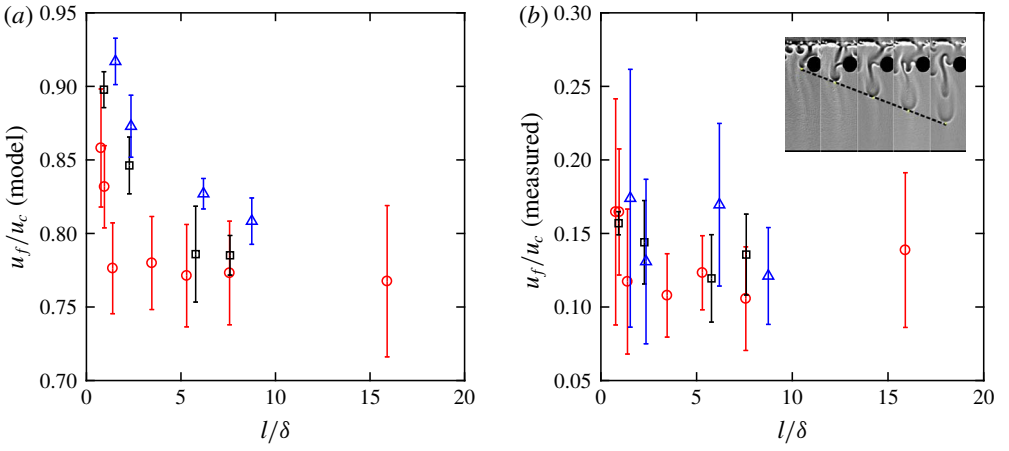


FIGURE 8. (Colour online) (*a*) Normalized finger velocity u_f/u_c calculated based on the number of fingers n_f and the incompressible flow condition (symbols represent different disc size D used in figure 7), and (*b*) u_f measured from a sequence of shadowgraph images as shown in the inset.

may exhibit a strong dependence on the disc configuration, and that parameter turns out to be the density contrast $\Delta\rho$ in Ra. In a homogeneous case with water above PPG, $\Delta\rho$ represents the density difference between the mixture at the interface with PPG. The addition of the disc layer separates the system into three layers, water, upper PPG layer above discs, and lower PPG layer below discs. If encountering discs, fingers have to turn around and mix with the rest of the upper PPG layer, effectively increasing the density of the upper PPG layer. Fingers going through the upper PPG layer will therefore experience smaller density contrast with the surrounding mixture.

For this reason, we define a new parameter – the effective Rayleigh number Ra_{eff} – to evaluate the change of the density contrast $\delta\rho = \rho_{in} - \rho_{out}$ between the liquids inside (ρ_{in}) and outside (ρ_{out}) of a finger. Figure 9(*a*) shows the calculated $Ra_{eff} = Sh/[c_w n_f(\delta/L)(u_f/u_c)]$ as a function of l/δ. The results are normalized by Ra using the maximum density difference $\Delta\rho$, so it should range from zero to one. An independent method is required to confirm that this calculated result indeed represents the finger density contrast $\delta\rho$. In this study, $\delta\rho$ is also indirectly inferred from the intensity contrast of a finger in a shadowgraph image (MacBeth & Thompson 1951). As shown in figure 9(*c*), the intensity of a horizontal line of pixels right below the disc layer is obtained from shadowgraph images. Each finger can be identified by its feature as two peaks with a valley in between (Settles 2012). The intensity difference between the peak and valley defines the intensity contrast ΔI, which provides a way to evaluate the density contrast indirectly. In figure 9(*c*), two intensity profiles from two experiments with the same disc size $D = 2.5$ mm but different l/δ (0.77 and 5.30) are shown. It is clear that, even though there are more fingers for $l/\delta = 5.30$, the ΔI of these fingers are not as strong as those for $l/\delta = 0.77$.

Figure 9(*b*) shows the variations of ΔI as a function of l/δ. The trend appears to be similar to that of Ra_{eff} shown in figure 9(*a*). Both Ra_{eff} and ΔI have non-monotonic dependences on l/δ, and there is a transition near $l/\delta = 1 \sim 3$. These similarities imply that the trend of the calculated Ra_{eff} can indeed characterize the density gradient of a finger in different configurations.

https://doi.org/10.1017/jfm.2018.732 Published online by Cambridge University Press

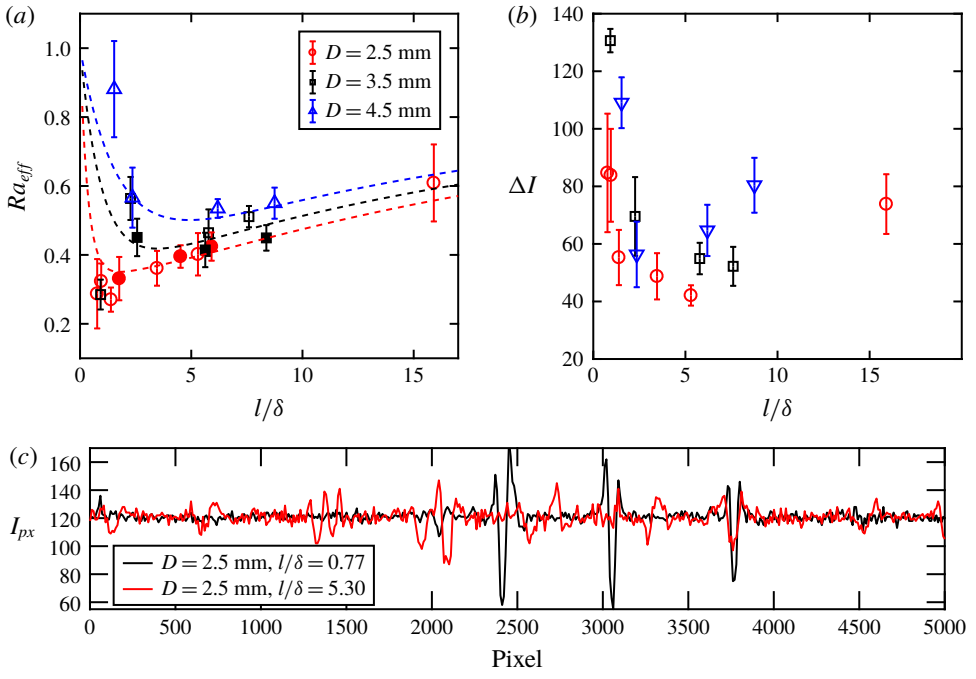


FIGURE 9. (Colour online) (*a*) The effective Rayleigh number Ra_{eff} calculated from $Sh/[c_w n_f(\delta/L)(u_f/u_c)]$ versus different disc spacings l/δ, (*b*) the intensity contrast ΔI of fingers extracted from the intensity profile shown in (*c*), and (*c*) the intensity profile of a horizontal line of pixels located right below the disc layer in a shadowgraph image.

This finding raises more questions as to why the density contrast of fingers experiences a transition that depends on the disc spacing l. As suggested before, this is primarily because the disc spacing controls the mixing in the upper PPG layer.

When $l/\delta \gg 1$, most fingers from the water–PPG interface can directly pass through the disc layer. The density contrast of these fingers recovers that of the homogeneous case: $\delta\rho = \Delta\rho$. When the number of discs increases and l decreases, some fingers start to hit discs and are forced to return and mix with the remaining PPG in the upper PPG layer. This forced mixing will effectively increase the density of the background fluid for other fingers and reduces the finger density contrast. Based on this, we argue that $\delta\rho$ is inversely proportional to the probability of a finger encountering a disc. This probability is related to the number of discs $N_D = L/(l+D)$. In addition, the functional form linking $\delta\rho$ and N_D has to satisfy two limiting cases for $l = 0$ and $l = L$. So we choose $\delta\rho = c_2 \exp(-\beta N_D)$, which is bounded when N_D approaches zero or infinity.

For the other regime, when $l/\delta < 1$, the probability of a finger encountering a disc is no longer relevant to $\delta\rho$. For such a tight constraint, no fingers from the interface can cross the disc layer directly; all of them have to mix in the upper PPG layer and wait until the density of this layer becomes high enough to push some new fingers through those tight constraints. That explains why $\delta\rho$ increases with decreasing l/δ, as tighter constraints will require a higher density contrast to push the mixture through. To achieve bounded values at two limiting cases, we again model $\delta\rho = c_1 \exp(-\alpha l/\delta)$.

https://doi.org/10.1017/jfm.2018.732 Published online by Cambridge University Press

The superposition of these two extreme limits helps to model the trend of Ra_{eff} versus l/δ from $l/\delta = 0$ to L/δ:

$$Ra_{eff} = C_1 \left[\exp\left(-\alpha \frac{l}{\delta}\right) + C_2 \exp\left(-\beta \frac{L/\delta}{l/\delta + D/\delta}\right) \right] + C_3. \tag{4.1}$$

The second exponential term can also be written as $C_2 \exp[-\beta(H/D)(L/l)\Omega]$, where $\Omega = (D/H)/(k_l/k)$ and $k_l/k \approx l/(l+D)$. Thus Ra_{eff} becomes a complicated function of both l/δ and Ω, so it cannot be collapsed by either one alone. This model emphasizes the importance of the disc spacing l in controlling the mixing process and the dissolution mass transfer rate. More importantly, l plays an opposite role in two different regimes separated by $l/\delta \approx 1$, which is surprising but successfully captured by our model. Note that, although there are five parameters, they are not all independent: C_2 and C_3 are determined from a combination of three other parameters by imposing the conditions at two limiting cases at $l = 0$ and $l = L$. In both cases when the disc layer is completely closed at $l = 0$ or completely open at $l = L$, the finger density contrast $\delta\rho$ should recover the largest density contrast $\Delta\rho$, and the normalized Ra_{eff} goes to one.

The dashed lines in figure 9(*a*) show the modelled Ra_{eff} following (4.1). Three parameters, C_1, α and β, in the model are fitted to these data points; C_2 is found to be close to one. Since C_2 controls the relative weight of two exponential functions, it suggests that both mixing mechanisms are equally important for the intermediate range of $l/\delta \approx 1$. For three different disc sizes, β, C_2 and C_3 are in a similar range (0.1–1). On the other hand, C_1 and α exhibit relatively stronger dependences on disc sizes, even though the values are still around the order of unity. In addition, since the two exponential terms have the opposite dependences on l/δ, once l/δ crosses from one regime to the other, one term will become dominant over the other one and control the Ra_{eff} dependence very quickly.

Equation (4.1) can also be used to confirm the Sherwood-number dependence by multiplying Ra_{eff} with the exponential fit of n_f and functional form of u_f/u_c derived from the incompressible flow conditions. The results are shown in figure 6(*b*) as dashed lines, which seem to collapse well with the experimental results and show a clear transition near $l/\delta = 1$. It is important to emphasize that, although $\delta\rho$ tends to increase with decreasing l when $l/\delta < 1$, the overall dissolution rate decreases sharply in this regime, because increasing $\delta\rho$ is not sufficient to compensate for significantly fewer fingers through the disc layer.

4.2.3. *Interface position*

Finally, the effect of relative distance h from the water–PPG interface to the disc layer will be discussed. For h, there are two extreme cases, $h = 0$ and $h = H$. At $h = 0$, the disc layer directly touches the interface, so it becomes challenging to control and monitor the disc–interface interaction. We decided to start with $h = 3\delta$ (2 mm), which is away from the interface so that the disc does not interfere with the boundary layer dynamics. All the discussions so far are based on disc configurations at this constant $h = 3\delta$. The other limit is at $h = H$. For this case, the disc is at the bottom of the PPG layer, and it will contribute very little to the fingering dynamics. In order to investigate how the Sherwood number transitions from one limit to the other, we have systematically investigated the dependence of Sh on h.

As shown in figure 10(*a*), the interface height rises as a function of time for four different h values. But instead of having one linear line, all curves show a rather

https://doi.org/10.1017/jfm.2018.732 Published online by Cambridge University Press

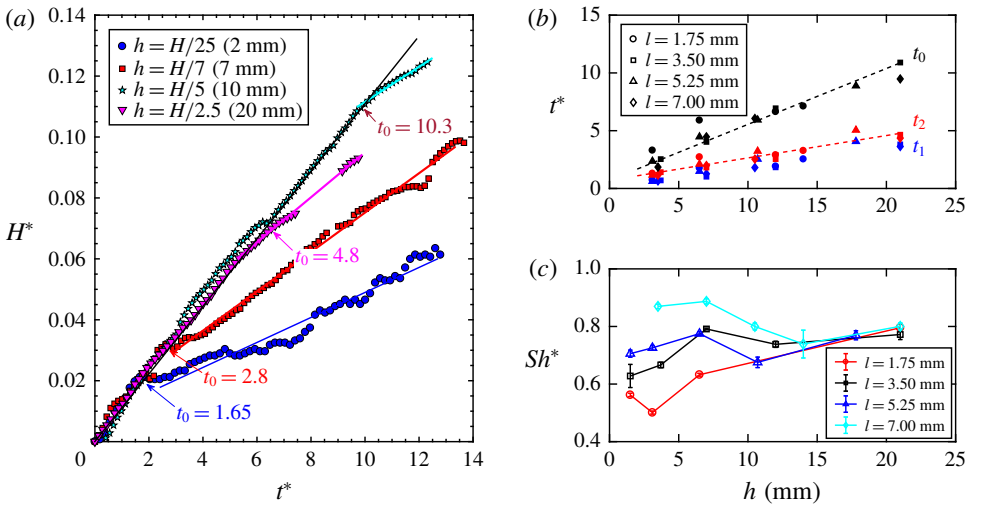


FIGURE 10. (Colour online) (*a*) The normalized interface location versus time. Arrows point at the transition time t_0 between two linear regimes with different slopes. (*b*) The transition time t_0 (black), as well as the time that it takes for mixture fingers travelling from the water–PPG interface to the top (t_1, blue) and bottom (t_2, red) of the disc layer, are shown as functions of the separation h between the disc layer and the interface. The two dashed lines are linear fits to red and black symbols, respectively. The slopes of these two lines differ by a factor of 2.5. (*c*) The normalized Sherwood number as a function of h for different disc spacings l.

sharp transition from one linear regime to another. Before the transition, all curves seem to collapse onto one line, as indicated by the black solid line. The slope of this line recovers that of the homogeneous configuration with no discs, indicating that the dynamics in the very beginning tends to be the same until the system starts to sense the existence of the disc layer. After the transition, the slope drops significantly, suggesting a sudden reduction of the mass transfer rate. The transition time t_0 appears to increase with h. To confirm that, t_0 for different h and l is shown in figure 10(*b*) (black symbols) for different disc configurations. It seems that t_0 increases linearly with respect to h.

The results suggest that the presence of the disc layer will not be sensed until the first group of fingers touch the disc layer after travelling a distance h from the interface. If the travelling speed of the fingers in all configurations stays the same, the transition time t_0 will increase linearly with h. In figure 10(*b*), in addition to t_0, the average times for fingers to travel from the interface to the top (t_1, blue) and bottom (t_2, red) of the disc layer are also shown. These two time delays are extracted from the shadowgraph movies. Times t_1 and t_2 are close to each other, and both of them depend linearly on h, indicating that fingers travel indeed at a constant speed independent of h. But the slopes of t_1 and t_2 with respect to h are smaller than that of the transition time t_0. In figure 10(*b*), two dashed lines show linear fits of t_0 and t_2. The slopes of these two lines differ roughly by a factor of 2.5, i.e. $t_0 = 2.5t_2$ for all disc configurations. Note that the convective mass transfer rate is measured by detecting the interface rising velocity. Although fingers take time t_2 to travel to the disc layer, it might take another time t_2 to bring the disc layer effect back to the interface by those turn-around

https://doi.org/10.1017/jfm.2018.732 Published online by Cambridge University Press

fingers to complete the mixing. Adding these two travelling times together will give us $\sim 2t_2$, which approximates a factor of 2.5 difference between t_0 and t_2.

From those lines shown in figure 10(*a*), the slopes of the curves after the transition are used to calculate Sh^*, and their dependences on h are shown in figure 10(*c*). The Sh^* value shows a strong dependence on l at small h, but it becomes less sensitive to l as the disc layer moves away from the interface. If that is the only effect, as h increases, Sh^* for all l should increase monotonically until they reach one. However, when h increases from 0 to 10 mm, Sh^* at large l (e.g. $l = 7$ mm in figure 10*c*) decreases and collapses with the curve at a smaller $l = 1.75$ mm. This is driven by another competing effect at play. When h increases, δ grows as well due to diffusion and merging, resulting in a small l/δ even for a large l. Based on our discussions on figure 6, a reduced l/δ leads to a smaller Sh^*, which will cause the Sh^*–h curve for a large l to go down. This effect is more important for large l, which explains the observed non-monotonic dependence of Sh^* as h increases for $l = 7.0$ mm.

5. Summary

In this paper, we have conducted experimental investigations to study the dissolution-driven convection in a heterogeneous and anisotropic porous medium. A disc layer with alternating low- and high-permeability gaps is introduced, and the disc size (D) and disc spacing (l) were systematically varied in order to study the dependence of the dimensionless mass transfer rate, i.e. Sh, on those parameters. Since the flow obeys Darcy's law, it was expected that Sh should depend on the mean permeability of the disc layer. Instead, Sh depends primarily on the disc spacing l (the high-permeability gaps).

When l is normalized by the finger width δ, Sh shows a clear transition $l/\delta \approx 1$, which determines if the disc spacing is wide enough to allow fingers to pass. To explain the dependence of Sh with l/δ, the convective mass transfer rate is decoupled into the number (n_f), velocity (u_f) and density contrast ($\delta\rho$) of fingers that pass through the disc layer. To our surprise again, despite the dependence of Sh on l/δ, n_f can only be collapsed by the mean permeability of the disc layer.

This difference is finally attributed to a complex dependence of $\delta\rho$ on both l/δ and the layer permeability. To facilitate our discussions, $\delta\rho$ of fingers is replaced by an effective Rayleigh number Ra_{eff}. Two independent methods have been used to estimate the trend of Ra_{eff}: (1) Sh divided by n_f and u_f/u_c and (2) intensity contrast of fingers using shadowgraph images. These results show a consistent picture that the density of fingers is sensitive to the mixing of PPG above the disc layer. For $l/\delta > 1$, the mixing is determined by the frequency of fingers encountering discs, as these fingers, once they hit discs, will be forced to turn around and mix with PPG. For $l/\delta < 1$, all fingers have to mix in the upper PPG layer because the gap size is too small for any finger to pass through directly. In this regime, the mixing is insensitive to disc size or permeability but completely dominated by the disc spacing l. A model is developed based on this observation and it also satisfies two limiting cases at $l = 0$ and $l = L$. The model shows nice agreement with the overall trend of Ra_{eff} as well as Sh.

Finally, the effect of the separation between the water–PPG interface to the disc layer h has also been studied. It turns out that the mass transfer experiences a sharp transition from a homogeneous no-disc case to a value that is significantly smaller. The transition time delays linearly with h and is proportional to the time that it takes for a finger to travel from the interface to the disc layer and back to the interface. It is also found that the effect of a disc layer becomes not only delayed but also weakened

https://doi.org/10.1017/jfm.2018.732 Published online by Cambridge University Press

as h increases. Intuitively, as the disc layer moves away from the interface, Sh should continue to increase until it reaches that of the homogeneous case. However, there is another competing effect – the growing finger width as h increases. A disc layer with the same disc spacing but located farther away from the interface is more difficult for a wider finger to pass, leading to a reduced Sh. These two effects combined create a non-trivial Sh–h dependence.

In summary, we conducted an experimental investigation of the dissolution convection in a porous medium with multiscale heterogeneity. Distinct from previous work, the results show a complicated dependence not only on the permeability, but also on the imposed length scales. The couplings among these new length scales with the inherent length scales from the convection drives mixing and mass transfer in a rather complicated way that one might not expect. Our results present important implications to future estimation of subsurface carbon sequestration with natural multiscale heterogeneity.

Acknowledgement

Acknowledgment is made to the Donors of the American Chemical Society Petroleum Research Fund (57751-DNI9) for partial support of this research.

Appendix

This appendix provides details on estimating the permeability of a Hele-Shaw cell with and without a disc layer. The permeability of the disc layer alone is k_l and the remaining homogeneous medium has permeability k. Both k and k_l can be evaluated from Darcy's law: $k = \mu u/\nabla p$, where μ is the fluid viscosity. The permeability change is small and is challenging to measure experimentally without having a new set-up with precise control. To overcome this problem, we decided to use simulations to estimate the permeability of the single layer. Since the flow is in the Stokes flow limit, the simulation should provide an accurate estimation with small computational cost. For simplicity, we chose to use the commercial computational fluid dynamics software ANSYS Fluent. Simulations were set up in a three-dimensional domain, matched exactly to experiments. In order to validate the numerical results, we first conducted the simulation in a homogeneous case without discs. The fluid used in these simulations was PPG and it was subjected to a uniform pressure gradient: $\nabla p = \rho_{PPG} g$. The homogeneous case was used to validate the simulation, and the numerical results turn out to match perfectly with the analytic calculation $k = b^2/12$.

After this validation, we performed the same simulation but limited to the disc layer alone. The simulations were repeated for different configurations. In figure 11, the normalized disc layer permeability $\pi = k_l/k$ is shown and it matches almost perfectly with the functional form $l/(l + D)$ that is related to the fraction of the opening in the disc layer. At the opening between discs, the permeability is still $k = b^2/12$, controlled primarily by the gap width b. The resulting flow rate u through such an opening should be the same as that in a homogeneous case under the same pressure gradient. But the mean flow rate across the disc layer has to average both the opening and impermeable discs $\langle u \rangle = ul/(l + D)$. With the same pressure head and viscosity, it is not surprising that the mean permeability of the disc layer is $k_l = l/(l + D)k$.

The permeability k_l is that of the disc layer. If the simulation is extended to the entire cell height with a disc layer inside, the permeability calculated becomes a mean value. Since the disc layer is rather thin, approximately 10 % of H, the addition of discs was found to affect the bulk permeability k by less than 10 %.

https://doi.org/10.1017/jfm.2018.732 Published online by Cambridge University Press

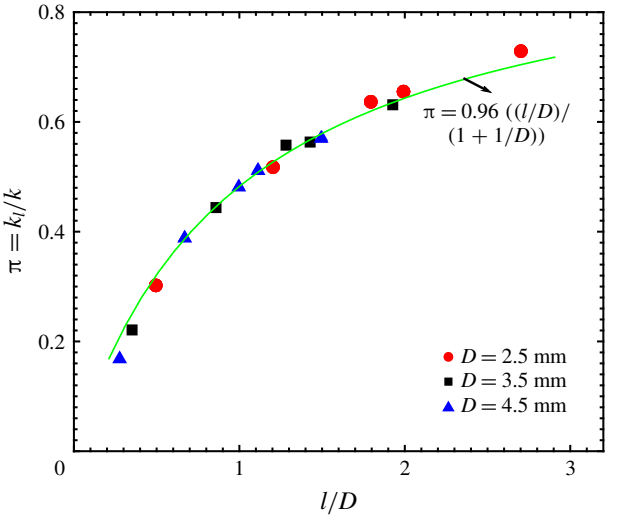


FIGURE 11. (Colour online) The normalized disc layer permeability $\pi = k_l/k$ as a function of the disc layer spacing (l/D).

REFERENCES

AGARTAN, E., TREVISAN, L., CIHAN, A., BIRKHOLZER, J., ZHOU, Q. & ILLANGASEKARE, T. H. 2015 Experimental study on effects of geologic heterogeneity in enhancing dissolution trapping of supercritical CO_2. *Water Resour. Res.* **51** (3), 1635–1648.

BACKHAUS, S., TURITSYN, K. & ECKE, R. E. 2011 Convective instability and mass transport of diffusion layers in a Hele-Shaw geometry. *Phys. Rev. Lett.* **106** (10), 104501.

CAVANAGH, A. J. & HASZELDINE, R. S. 2014 The Sleipner storage site: capillary flow modeling of a layered CO_2 plume requires fractured shale barriers within the Utsira Formation. *Intl J. Greenh. Gas Control* **21**, 101–112.

CHENG, P., BESTEHORN, M. & FIROOZABADI, A. 2012 Effect of permeability anisotropy on buoyancy-driven flow for CO_2 sequestration in saline aquifers. *Water Resour. Res.* **48** (9), W09539.

ECKE, R. E. & BACKHAUS, S. 2016 Plume dynamics in Hele-Shaw porous media convection. *Phil. Trans. R. Soc. Lond.* A **374** (2078), 20150420.

ELENIUS, M. T. & JOHANNSEN, K. 2012 On the time scales of nonlinear instability in miscible displacement porous media flow. *Comput. Geosci.* **16** (4), 901–911.

EMAMI-MEYBODI, H., HASSANZADEH, H., GREEN, C. P. & ENNIS-KING, J. 2015 Convective dissolution of CO_2 in saline aquifers: progress in modeling and experiments. *Intl J. Greenh. Gas Control* **40**, 238–266.

ENNIS-KING, J., PRESTON, I. & PATERSON, L. 2005 Onset of convection in anisotropic porous media subject to a rapid change in boundary conditions. *Phys. Fluids* **17** (8), 084107.

FARAJZADEH, R., MEULENBROEK, B., DANIEL, D., RIAZ, A. & BRUINING, J. 2013 An empirical theory for gravitationally unstable flow in porous media. *Comput. Geosci.* **17** (3), 515–527.

FARAJZADEH, R., RANGANATHAN, P., ZITHA, P. L. J. & BRUINING, J. 2011 The effect of heterogeneity on the character of density-driven natural convection of CO_2 overlying a brine layer. *Adv. Water Resour.* **34** (3), 327–339.

FOSTER, T. D. 1965 Stability of a homogeneous fluid cooled uniformly from above. *Phys. Fluids* **8** (7), 1249–1257.

GREEN, C. P. & ENNIS-KING, J. 2014 Steady dissolution rate due to convective mixing in anisotropic porous media. *Adv. Water Resour.* **73**, 65–73.

https://doi.org/10.1017/jfm.2018.732 Published online by Cambridge University Press

HASSANZADEH, H., POOLADI-DARVISH, M. & KEITH, D. W. 2007 Scaling behavior of convective mixing, with application to geological storage of CO_2. *AIChE J.* **53** (5), 1121–1131.

HEWITT, D. R. 2014 High Rayleigh number convection in a porous medium. PhD thesis, University of Cambridge.

HEWITT, D. R., NEUFELD, J. A. & LISTER, J. R. 2012 Ultimate regime of high Rayleigh number convection in a porous medium. *Phys. Rev. Lett.* **108** (22), 224503.

HEWITT, D. R., NEUFELD, J. A. & LISTER, J. R. 2014 High Rayleigh number convection in a porous medium containing a thin low-permeability layer. *J. Fluid Mech.* **756**, 844–869.

HIDALGO, J. J. & CARRERA, J. 2009 Effect of dispersion on the onset of convection during CO_2 sequestration. *J. Fluid Mech.* **640**, 441–452.

HIDALGO, J. J., FE, J., CUETO-FELGUEROSO, L. & JUANES, R. 2012 Scaling of convective mixing in porous media. *Phys. Rev. Lett.* **109** (26), 264503.

HORTON, C. W. & ROGERS, F. T. JR. 1945 Convection currents in a porous medium. *J. Appl. Phys.* **16** (6), 367–370.

HUBEL, A., BIDAULT, N. & HAMMER, B. 2002 Transport characteristics of glycerol and propylene glycol in an engineered dermal replacement. In *ASME 2002 International Mechanical Engineering Congress and Exposition*, pp. 121–122. American Society of Mechanical Engineers.

HUPPERT, H. E. & NEUFELD, J. A. 2014 The fluid mechanics of carbon dioxide sequestration. *Annu. Rev. Fluid Mech.* **46**, 255–272.

LAPWOOD, E. R. 1948 Convection of a fluid in a porous medium. In *Mathematical Proceedings of the Cambridge Philosophical Society*, vol. 44, pp. 508–521. Cambridge University Press.

MACBETH, G. & THOMPSON, A. R. 1951 Densities and refractive indexes for propylene glycol–water solutions. *Analyt. Chem.* **23** (4), 618–619.

MCKIBBIN, R. & O'SULLIVAN, M. J. 1980 Onset of convection in a layered porous medium heated from below. *J. Fluid Mech.* **96** (2), 375–393.

MCKIBBIN, R. & O'SULLIVAN, M. J. 1981 Heat transfer in a layered porous medium heated from below. *J. Fluid Mech.* **111**, 141–173.

MEYBODI, H. E. & HASSANZADEH, H. 2013 Mixing induced by buoyancy-driven flows in porous media. *AIChE J.* **59** (4), 1378–1389.

NEUFELD, J. A., HESSE, M. A., RIAZ, A., HALLWORTH, M. A., TCHELEPI, H. A. & HUPPERT, H. E. 2010 Convective dissolution of carbon dioxide in saline aquifers. *Geophys. Res. Lett.* **37** (22), L22404.

NIELD, D. A. 1983 The boundary correction for the Rayleigh–Darcy problem: limitations of the Brinkman equation. *J. Fluid Mech.* **128**, 37–46.

NIELD, D. A. & BEJAN, A. 2006 *Convection in Porous Media*, vol. 3. Springer.

OTERO, J., DONTCHEVA, L. A., JOHNSTON, H., WORTHING, R. A., KURGANOV, A., PETROVA, G. & DOERING, C. R. 2004 High-Rayleigh-number convection in a fluid-saturated porous layer. *J. Fluid Mech.* **500**, 263–281.

PAU, G. S. H., BELL, J. B., PRUESS, K., ALMGREN, A. S., LIJEWSKI, M. J. & ZHANG, K. 2010 High-resolution simulation and characterization of density-driven flow in CO_2 storage in saline aquifers. *Adv. Water Resour.* **33** (4), 443–455.

RAHBARI-SISAKHT, M., TAGHIZADEH, M. & ELIASSI, A. 2003 Densities and viscosities of binary mixtures of poly(ethylene glycol) and poly(propylene glycol) in water and ethanol in the 293.15–338.15 K temperature range. *J. Chem. Engng Data* **48** (5), 1221–1224.

RAPAKA, S., PAWAR, R. J., STAUFFER, P. H., ZHANG, D. & CHEN, S. 2009 Onset of convection over a transient base-state in anisotropic and layered porous media. *J. Fluid Mech.* **641**, 227–244.

REES, D. A. S. & BASSOM, A. P. 2000 The onset of Darcy–Bénard convection in an inclined layer heated from below. *Acta Mechanica* **144** (1–2), 103–118.

REES, D. A. S. & GENÇ, G. 2011 The onset of convection in porous layers with multiple horizontal partitions. *Intl J. Heat Mass Transfer* **54** (13–14), 3081–3089.

REES, D. A. S. & RILEY, D. S. 1990 The three-dimensional stability of finite-amplitude convection in a layered porous medium heated from below. *J. Fluid Mech.* **211**, 437–461.

https://doi.org/10.1017/jfm.2018.732 Published online by Cambridge University Press

SETTLES, G. S. 2012 *Schlieren and Shadowgraph Techniques: Visualizing Phenomena in Transparent Media*. Springer.

SLIM, A. C. 2014 Solutal-convection regimes in a two-dimensional porous medium. *J. Fluid Mech.* **741**, 461–491.

SLIM, A. C. & RAMAKRISHNAN, T. S. 2010 Onset and cessation of time-dependent, dissolution-driven convection in porous media. *Phys. Fluids* **22** (12), 124103.

SZULCZEWSKI, M. L., HESSE, M. A. & JUANES, R. 2013 Carbon dioxide dissolution in structural and stratigraphic traps. *J. Fluid Mech.* **736**, 287–315.

XU, X., CHEN, S. & ZHANG, D. 2006 Convective stability analysis of the long-term storage of carbon dioxide in deep saline aquifers. *Adv. Water Resour.* **29** (3), 397–407.

https://doi.org/10.1017/jfm.2018.732 Published online by Cambridge University Press